

Synergistic Regulation of Phonon and Electronic Properties to Improve the Thermoelectric Performance of Chalcogenide $\text{CuIn}_{1-x}\text{Ga}_x\text{Te}_2:\text{yInTe}$ ($x = 0-0.3$) with In Situ Formed Nanoscale Phase InTe

Min Li, Yong Luo,* Xiaojuan Hu, Gemei Cai, Zhongkang Han,* Zhengliang Du, and Jiaolin Cui*

Most ternary Cu-In-Te chalcogenides have large bandgaps and high Seebeck coefficients, hence they have received much attention in the thermoelectric (TE) community. However, it is still challenging to reduce their thermal conductivities while sustaining their electrical properties; therefore, much work needs to be done. The phonon and electronic properties in ternary CuInTe_2 -based chalcogenides $\text{CuIn}_{1-x}\text{Ga}_x\text{Te}_2:\text{yInTe}$ ($x = 0-0.3$) with in situ formed nanoscale phase InTe precipitated in the grain boundaries is synergistically regulated. This regulation reduces the lattice thermal conductivity by a factor of ≈ 2 compared to pristine CuInTe_2 , due to phonon–phonon interaction and point defect scatterings introduced in the main phase at high temperatures for samples at $x \leq 0.2$, combined with the phonon blocking effect from InTe at low and middle temperatures. At the same time, the power factor enhances by 73%. As a result, the TE performance improves significantly with a peak figure of merit value of 1.22 at ≈ 850 K.


Dr. M. Li, Z. Du, Prof. J. Cui
School of Materials and Chemical Engineering
Ningbo University of Technology
Ningbo 315211, China
E-mail: cuijiaolin@163.com

Dr. M. Li, Prof. Y. Luo
School of Materials Science and Engineering
China University of Mining and Technology
Xuzhou 221116, China
E-mail: sulyflying@cumt.edu.cn

Dr. X. Hu, Dr. Z. Han
Theory Department
Fritz Haber Institute of the Max-Planck-Society
Faradayweg 4–6, D-14195 Berlin, Germany
E-mail: han@fhi-berlin.mpg.de

Prof. G. Cai
School of Materials Science and Engineering
Central South University
Changsha 410083, China

Dr. Z. Han
Center for Energy Science and Technology
Skolkovo Institute of Science and Technology
Moscow 413026, Russia

 The ORCID identification number(s) for the author(s) of this article can be found under <https://doi.org/10.1002/aelm.201901141>.

© 2020 The Authors. Published by WILEY-VCH Verlag GmbH & Co. KGaA, Weinheim. This is an open access article under the terms of the Creative Commons Attribution License, which permits use, distribution and reproduction in any medium, provided the original work is properly cited.

DOI: 10.1002/aelm.201901141

1. Introduction

Thermoelectric (TE) materials can generate electricity from low-grade waste heat. The efficiency of TE materials is determined by the dimensionless figure of merit figure of merit (ZT) = $\alpha^2\sigma T/\kappa$, here α is the Seebeck coefficient, σ the electrical conductivity, T the absolute temperature, and κ the thermal conductivity consisting of electronic (κ_e) and lattice (κ_l) parts mainly. In order to obtain a high ZT value, the materials should have high power factors (PF), $\text{PF} = \alpha^2\sigma$, and at the same time low thermal conductivities (κ). However, the three parameters α , σ , and κ_e are interrelated and all dependent on the carrier concentration n , thus making it challenging to decouple them.

Ternary CuInTe_2 compound with a chalcopyrite structure has recently received much attention in thermoelectrics in a sense that it has a high Seebeck coefficient ($\approx 400 \mu\text{VK}^{-1}$) and optimal carrier concentration n (10^{18} – 10^{19}cm^{-3}) at room temperature (RT).^[1–3] Besides, its direct bandgap ($\approx 1.05 \text{eV}$)^[4] is much larger than those of traditional TE materials, for example, 0.11 eV for Bi_2Te_3 ,^[5] 0.14 eV for Sb_2Te_3 ,^[6] and 0.18 eV for PbTe ,^[7] which prevent the degradation of the thermoelectric performance from the thermally activated minority carriers at high temperatures.^[8] However, this compound gives a relatively high thermal conductivity with the κ_l value of 4.0–7.0 $\text{W m}^{-1} \text{K}^{-1}$ at RT and 1.0–1.3 $\text{W m}^{-1} \text{K}^{-1}$ at ≈ 850 K,^[1,2,9] therefore, the TE performance of the pristine CuInTe_2 is still low, evidenced by many experiments with the ZT value being only 0.24–0.76.^[2,10,11]

To improve the TE performance of the materials, many effective strategies have been employed, guided by the phonon-glass-electron crystal (PGEC) proposal.^[12] The typical examples include the band structure engineering involving the band degeneracy^[13,14] and distortion,^[15] introductions of nanoparticles of magnetic materials^[16–18] or carrier–magnetic moment interaction,^[19] to enhance the power factor $\alpha^2\sigma$, or the microstructure engineering including the introductions of all-scale hierarchical architectures^[20–23] and the point defects^[24–28] to reduce the lattice part κ_l . Owing to the presence of crystal-field

Δ_{CF} splitting and spin-orbit Δ_{SO} effect,^[4] the crystal structure engineering, which is successfully employed in the Ag(Zn)-introduced CuInTe_2 compound systems,^[29,30] may be an alternative way to reduce the lattice κ_L . Unfortunately, the power factors do not increase significantly. In contrast, Luo et al. succeed in enhancing the power factor (PF) from $8.3 \mu\text{W m}^{-1} \text{K}^{-2}$ (at $\approx 700 \text{ K}$) to $14.45 \mu\text{W m}^{-1} \text{K}^{-2}$ (at $\approx 500 \text{ K}$) through introducing a nanoscale phase (In_2O_3) in CuInTe_2 ^[31]; however, the lattice parts κ_L do not reduce largely.^[31,32]

Recently, we have developed several kinds of Cu-In-Te derivatives, such as $(\text{Cu}_2\text{Te})_\delta\text{Cu}_{1.15}\text{In}_{2.29}\text{Te}_4$ ($\delta = 0-0.075$),^[33] $\text{Cu}_{2.5} + \delta\text{In}_{4.5}\text{Te}_8$ ($\delta = 0-0.15$),^[34] and $(\text{Cu}_2\text{Te})_x(\text{Cu}_{3.52}\text{In}_{4.16}\text{Te}_8)$ ^[35] and reduced their lattice part κ_L to $0.3 \text{ W K}^{-1} \text{ m}^{-1}$.^[35] However, the TE performance of these materials does not still fully optimize as the highest PF value is only $3.82-10.59 \mu\text{W m}^{-1} \text{K}^{-2}$.^[33-35] This implies that, to our best knowledge, the versatility of the ternary Cu-In-Te chalcogenides as TE candidates has not been explored to the fullest to date.

In order to resolve the dichotomy between the high power factor and low thermal conductivity in ternary Cu-In-Te chalcogenides, we in this work develop another kind of Cu-In-Te derivative system $\text{CuIn}_{1-x}\text{Ga}_x\text{Te}_2:\gamma\text{InTe}$, aiming to enhance the power factor through the electronic structure regulation, and at the same time reducing the lattice part κ_L through introductions of multi-scale phonon blocking barriers in the matrix. After implementing this strategy, the power factor increases to $13.8 \mu\text{W m}^{-1} \text{K}^{-2}$ at $\approx 687 \text{ K}$, about 73% enhancement compared to the pristine CuInTe_2 ,^[31] and at the same time the lattice part κ_L reduces to $0.61 \text{ W m}^{-1} \text{K}^{-1}$ at $\approx 854 \text{ K}$, decreasing by a factor of 2.^[36] The results provide strong evidence that the synergistic regulation in the $\text{CuIn}_{1-x}\text{Ga}_x\text{Te}_2:\gamma\text{InTe}$ chalcogenide is an effective strategy.

2. Results and Discussion

2.1. Refinements of the X-Ray Diffraction Patterns

The Rietveld refinements of the powder X-ray diffraction (XRD) patterns of four $\text{CuIn}_{1-x}\text{Ga}_x\text{Te}_2:\gamma\text{InTe}$ samples ($x = 0, 0.1, 0.2, 0.3$) are shown in Figure S1, Supporting Information. The results, including the crystallographic data, Wyckoff positions, atomic coordinates, and site occupancy factors (SOFs), are listed in Tables S1–S11, Supporting Information. It is observed

that after the refinements the materials $\text{CuIn}_{1-x}\text{Ga}_x\text{Te}_2:\gamma\text{InTe}$ at $x = 0-0.2$ consist of the main phase CuInTe_2 (PDF:34–1498; s.g. I-42d) and in situ formed minor phase InTe (PDF:07–0112; s.g. I4/mcm), whose weight percents (γ) are 23.0 wt% ($x = 0$), 8.4 wt% ($x = 0.1$), and 5.3 wt% ($x = 0.2$). At $x = 0.3$ a pure phase CuInTe_2 was obtained without any second phase precipitated. The element Ga resides totally at the In site in the CuInTe_2 phase (see Tables S5, S8, and S11). In this regard, the chemical formulas can be expressed to be $\text{CuInTe}_2-23.0 \text{ wt}\%$ (InTe) for $x = 0$, $\text{CuIn}_{0.9}\text{Ga}_{0.1}\text{Te}_2-8.4 \text{ wt}\%$ (InTe) for $x = 0.1$, $\text{CuIn}_{0.8}\text{Ga}_{0.2}\text{Te}_2-5.3 \text{ wt}\%$ (InTe) for $x = 0.2$, and $\text{CuIn}_{0.7}\text{Ga}_{0.3}\text{Te}_2$ for $x = 0.3$.

The XRD patterns are summarized in Figure 1a, and the lattice constants a and c in $\text{CuIn}_{1-x}\text{Ga}_x\text{Te}_2$ are shown in Figure 1b, in which the two values decrease as the x value increases due to the smaller atomic Ga than that of In. In the in situ formed minor phase InTe , the elements In1 and In2 reside at In4a and 4b sites, and Te at the 16k site. The lattice constants of InTe fluctuate at 8.44 \AA in a and 7.14 \AA in c . Figure 1c is the cation-Te distances (d) and anion position displacement parameter u as a function of x value, where the d value of In-Te decreases, while that of Cu-Te remains almost unchanged. The u value fluctuates around 0.25, indicating that there is no big distortion of the crystal structure.^[37,38]

2.2. TE Performance and Transport Properties

TE properties of the $\text{CuIn}_{1-x}\text{Ga}_x\text{Te}_2:\gamma\text{InTe}$ ($x = 0-0.3$) chalcogenides are displayed in Figure 2, where the Seebeck coefficients (α) are positive over the entire temperature range (Figure 2a). The positive values indicate that the majority charges are p-type holes. Generally, the α value increases with increase in Ga content (x value), and it converges gradually above $\approx 680 \text{ K}$ at $x \leq 0.2$. At $x = 0.3$, the α values are much higher than those of the samples at $x \leq 0.2$ over the entire temperature range. The electrical conductivity (σ) increases as the x value increases before it starts to fall at $x > 0.2$, and at $x = 0.3$ the electrical conductivity decreases significantly, as shown in Figure 2b. Figure 2c showcases that the power factor ($\text{PF} = \alpha^2\sigma$) follows the trend of the electrical conductivity. The highest PF value is $13.8 \mu\text{W cm}^{-1} \text{K}^{-2}$ for the sample at $x = 0.2$ and 687 K . This value is much higher than those of most pure CuInTe_2 or its based chalcogenides

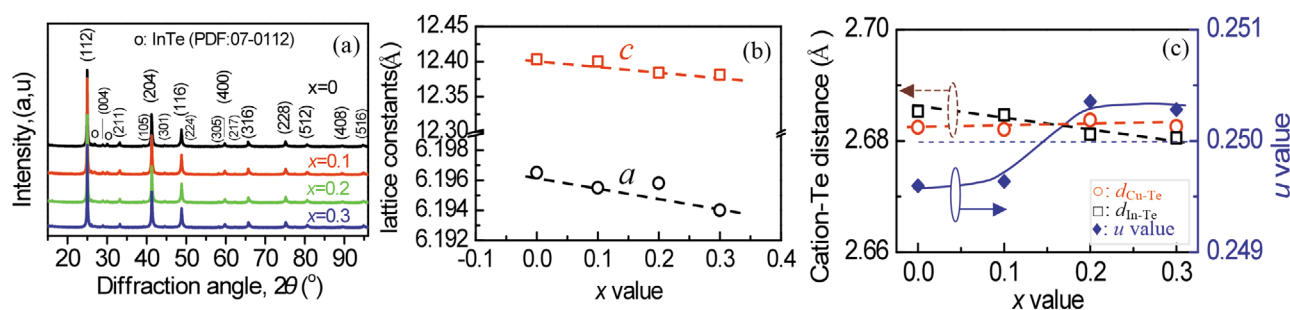


Figure 1. a) X-ray diffraction patterns of the materials $\text{CuIn}_{1-x}\text{Ga}_x\text{Te}_2:\gamma\text{InTe}$ ($x = 0-0.3$); b) Lattice constants a and c in $\text{CuIn}_{1-x}\text{Ga}_x\text{Te}_2$ ($x = 0-0.3$); c) Mean cation-Te (Cu-Te and In-Te) distances and anion position displacement value (u) as a function of x value in $\text{CuIn}_{1-x}\text{Ga}_x\text{Te}_2$.

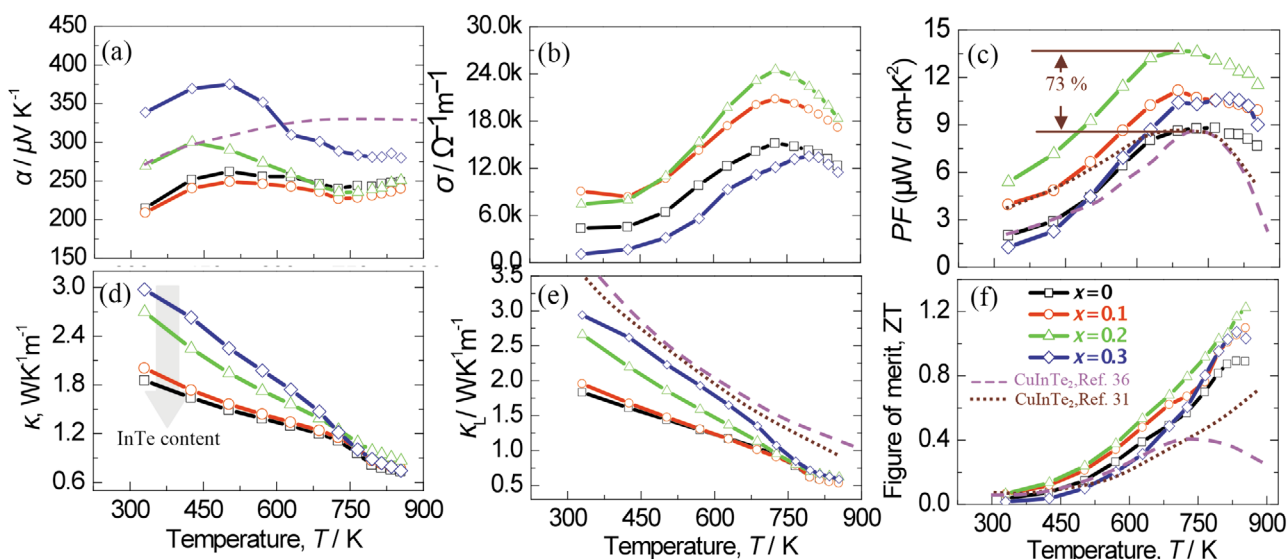


Figure 2. TE performance of the $\text{CuIn}_{1-x}\text{Ga}_x\text{Te}_2:y\text{InTe}$ ($x = 0-0.3$) chalcogenides. a) Seebeck coefficients (α) as a function of temperature; b) Electrical conductivities (σ) as a function of temperature; c) Power factors (PF) as a function of temperature; d) Total thermal conductivities (κ) as a function of temperature; e) Lattice thermal conductivity (κ_L) as a function of temperature; f) TE figure of merit (ZT), where the ZT values of the pristine CuInTe_2 from the literatures^[31,36] are shown for comparison.

reported ($3.82-11.7 \mu\text{W cm}^{-1} \text{K}^{-2}$)^[2,10,30,33-36,39-42] and comparable to those of $\text{Cu}_{0.95(6)}\text{InTe}_2$ ($13.0-13.7 \mu\text{W cm}^{-1} \text{K}^{-2}$)^[1,9] and $\text{Cu}_{0.95(6)}\text{InTe}_2 + \text{In}_2\text{O}_3$ ($14.45 \mu\text{W cm}^{-1} \text{K}^{-2}$)^[31]. However, the PF value is much lower than the estimated value of CuInTe_2 ($\text{PF} > 26 \mu\text{W cm}^{-1} \text{K}^{-2}$ at 800 K),^[43] suggesting that there is still a big room for the enhancement.

The total thermal conductivities (κ) are presented in Figure 2d as a function of temperature, where the κ values reduce with increase in temperature monotonically. Below ≈ 725 K the κ value increases as the x value increases. However, above ≈ 725 K it gradually converges and gets to the minimum value ($0.75-0.85 \text{ W m}^{-1} \text{K}^{-1}$). The lattice parts (κ_L) bear resemblance to the total κ and do not obey the classical T^{-1} relation below 725 K, as shown in Figure 2e. At 850 K the κ_L values converge to $\approx 0.55 \text{ W m}^{-1} \text{K}^{-1}$, which is $\approx 45\%$ lower than or half that of the pristine CuInTe_2 , signified in dotted lines.^[31,36]

Combined with the three parameters (α , σ , κ), we obtained the ZT values as a function of temperature (Figure 2f), where

the ZT values from ref. [31,36], signified in dotted lines are presented for comparison. It is observed that the ZT value increases as Ga content increases up to $x = 0.2$ with the peak value of 1.22 at ≈ 850 K. The ZT value is $\approx 73\%$ higher than^[31] or almost triple^[36] that of pristine CuInTe_2 , and stands high in the CuInTe_2 -based chalcogenides to date (see Figure 3a), proving that the synergistic regulation of phonon and electronic properties is successful in this work.

The notable and significant improvement in TE performance originates mainly from the enhanced power factor and reduced lattice thermal conductivity simultaneously. In order to gain a deep understanding of the associated transport properties, we have measured the Hall coefficients of the four samples ($x = 0-0.3$) near RT, and then calculated their Hall carrier concentrations (n_H) and mobility (μ). The results are shown in Figure 3b. It is observed that the n_H value enhances from $1.58 \times 10^{19} \text{ cm}^{-3}$ ($x = 0$) to the highest value $7.14 \times 10^{19} \text{ cm}^{-3}$ ($x = 0.3$), whereas the μ value exhibits an opposite trend, that is, it decays from $17.33 \text{ cm}^2 \text{ V}^{-1} \text{ s}^{-1}$ ($x = 0$)

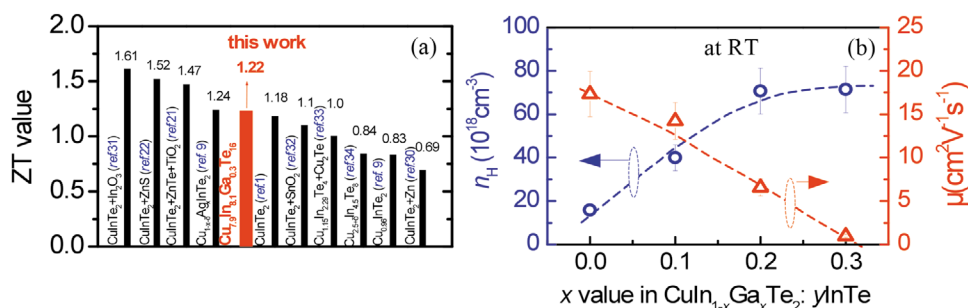


Figure 3. a) Comparison of the peak ZT value in the present work with those of the state-of-the-art ternary Cu-In-Te chalcogenides. b) The Hall carrier concentration (n_H) and mobility (μ) of $\text{CuIn}_{1-x}\text{Ga}_x\text{Te}_2:y\text{InTe}$ ($x = 0, 0.1, 0.2, 0.3$) as a function of Ga content (x value) at RT.

to the lowest value $0.96 \text{ cm}^2 \text{ V}^{-1} \text{ s}^{-1}$ ($x = 0.3$). It is therefore believed that the improvement in electrical conductivity is mainly attributed to the enhancement in carrier concentration. The decreasing of the σ value at $x = 0.3$ might be due to the increased scattering of the carriers at the point defect Ga_{In} in the solid solution $\text{Cu}_{7.9}\text{In}_{8.1}\text{Ga}_{0.3}\text{Te}_{16}$. Similarly, the Seebeck coefficient (α) is, on one hand, mainly governed by the enhanced density of the states (DOS) due to incorporation of Ga into the In site (see below), rather than by the barrier blocking effect^[44,45] in the heterojunction of $\text{InTe}/\text{CuIn}_{1-x}\text{Ga}_x\text{Te}_2$, since the extra phase boundaries tend to be diminished as the content of the minor phase InTe decreases to zero at $x = 0.3$. On the other hand, it is attributed to the increased effective mass (m^*) in CuInTe_2 upon Ga incorporation ($x < 0.3$), compared with those of CuInTe_2 -based chalcogenides whose α - n_{H} relation follows the single parabolic band (SPB) model (see later).

2.3. First-Principles Calculation

After XRD refinement, two phases $\text{CuIn}_{1-x}\text{Ga}_x\text{Te}_2$ and InTe are clearly observed, it is therefore necessary to know their roles in TE performance. Figure 4a,b represent the crystal structures of $\text{Cu}_{27}\text{In}_{33}\text{Te}_{64}$ and $\text{Cu}_{30}\text{In}_{30}\text{GaTe}_{64}$, established in terms of the XRD refinement results. It is observed that upon Ga incorporation the DOS near the Fermi level (E_f) increases compared to that of $\text{Cu}_{27}\text{In}_{33}\text{Te}_{64}$, as shown in Figure 4c, which is mainly attributed to the hybridization of the $\text{Te}5p$ - $\text{Cu}4s$ orbital. Although the contribution of the orbital Ga in both the VBM and CBM is limited, see the partial DOS in Figure 4d, its presence promotes to lift the valence band maximum (VBM) and to lower the conduction band minimum (CBM), thus narrowing the bandgap (E_g) (see Figure 4e,f). The increasing in DOS substantiates the increasing of the Seebeck coefficient,^[15] and the narrowing of the bandgap may stabilize the transport of carriers.^[46] Moreover, the simultaneous enhancement in α and n_{H} values implies that the material has a large effective mass (m^*). In order to confirm this assumption, we present the Pisarenko plot of the sample $\text{CuIn}_{1-x}\text{Ga}_x\text{Te}_2:\gamma\text{InTe}$ ($x = 0.3$) using the single parabolic band (SPB) model by taking an effective mass $m^{*0} = 2.7 m^0$ in Figure 5a, where the data circled in a wine dotted line is related to the pristine

CuInTe_2 that mostly obeys the Pisarenko relation (SPB model) from different experiments^[1,9,31,36,40,41,47] for comparison. It is observed that the α values from different experiments lie far below the Pisarenko relation. In comparison, the α values of the present composites $\text{CuIn}_{1-x}\text{Ga}_x\text{Te}_2:\gamma\text{InTe}$ ($x = 0, 0.1, 0.2$) (hollow symbols circled by shaded area) are much close to the Pisarenko line for the corresponding n_{H} values. This estimation, in accordance with the increasing of the DOS upon Ga addition, suggests the increasing of the effective mass (m^*) that plays a major role in contributing to the Seebeck coefficient. As a contrast, the impact of the barrier blocking in the heterojunction of $\text{InTe}/\text{CuIn}_{1-x}\text{Ga}_x\text{Te}_2$ on the Seebeck coefficient seems to be limited.

Figure 2d,e demonstrate the reduction tendency in total κ and lattice part κ_{L} as the InTe content increases below 725 K, guided by a gray arrow. Above 725 K, the thermal conductivities converge gradually. This appearance suggests that the thermal conduction at low and middle temperatures is not only affected by the low thermal conductivity of InTe itself ($\kappa_{\text{L}} = \approx 0.70$ and $0.47 \text{ W m}^{-1} \text{ K}^{-1}$ at 319 and 605 K),^[48] but also by the extra phonon scattering on the increased boundaries between InTe and $\text{CuIn}_{1-x}\text{Ga}_x\text{Te}_2$.

To gain a better understanding of this phenomenon, we calculate the lattice parts (κ_{L}^*) of the $\text{InTe}/\text{CuIn}_{1-x}\text{Ga}_x\text{Te}_2$ composites ($x \leq 0.2$) using the modified model (SCENT) by Hashin^[49] and Zhou^[36] below.

$$\frac{\kappa_{\text{L}}^* - \kappa^m}{\kappa_{\text{L}}^* + 2\kappa^m} = f \frac{\kappa^d - \kappa^m}{\kappa^d + 2\kappa^m} \quad (1)$$

Here κ^m and κ^d represent the thermal conductivities of matrix $\text{Cu}_{7.9}\text{In}_{8.1}\text{Ga}_{0.3}\text{Te}_{16}$ and in situ formed phase InTe , and κ_{L}^* stands for the effective values of the composites. The parameter f represents the molar fraction of InTe obtained from the γ values indicated in Section 2.1.

The estimated κ_{L}^* values in 319 and 605 K are presented in Figure 5b, where the κ_{L}^* data beyond 23 wt% InTe is not provided, as it is not the focus of our investigation. Nor are we able to calculate the κ_{L}^* data above 605 K as the thermal conductivities of the end member InTe above 605 K are not available.^[48] Based on the calculation using Equation (1), it is observed that the experimental κ_{L} values of $\text{CuInTe}_2:23 \text{ wt\% InTe}$ ($x = 0$) at 319 and 605 K are well below the calculation based on the

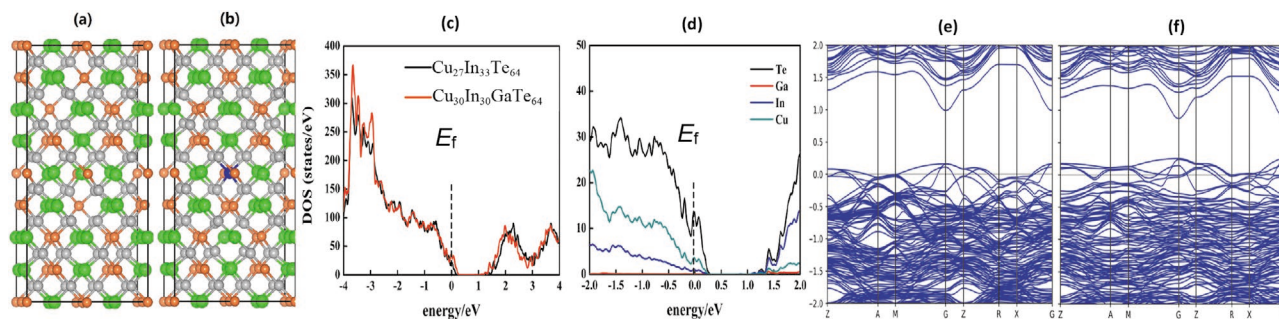


Figure 4. Crystal structures: a) $\text{Cu}_{27}\text{In}_{33}\text{Te}_{64}$ and b) $\text{Cu}_{30}\text{In}_{30}\text{GaTe}_{64}$, where Cu, In, Te, and Ga are in yellow, green, gray, and blue, respectively; The density of the states (DOS): c) $\text{Cu}_{27}\text{In}_{33}\text{Te}_{64}$ and $\text{Cu}_{30}\text{In}_{30}\text{GaTe}_{64}$; d) Partial DOS of Te, Ga, In, and Cu, which are in black, red, blue and green, respectively. Band structures of: e) $\text{Cu}_{27}\text{In}_{33}\text{Te}_{64}$ and f) $\text{Cu}_{30}\text{In}_{30}\text{GaTe}_{64}$.

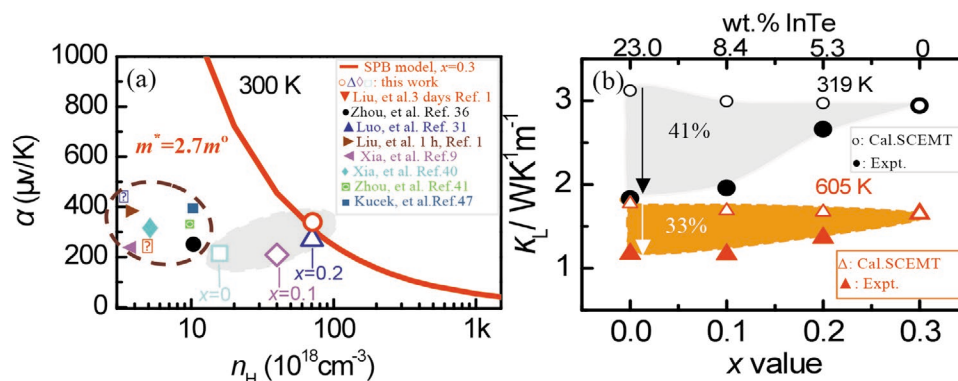


Figure 5. a) Pisarenko relation of the sample $\text{CuIn}_{0.7}\text{Ga}_{0.3}\text{Te}_2$ at 300 K using the single parabolic band model by taking an effective mass $m^* = 2.7 m^0$. The α - n_H relations in CuInTe_2 from different experiments reported^[1,9,31,36,40,41,47] (circled by wine dotted line) are presented for comparison with those of the present data (hollow symbols circled by gray shaded area); b) Lattice thermal conductivities at 319 and 605 K as a function of x value in $\text{CuIn}_{1-x}\text{Ga}_x\text{Te}_2$: γInTe , compared with the calculation data based on modified model (SCEMT) for the $(\text{CuIn}_{1-x}\text{Ga}_x\text{Te}_2)$: $\gamma(\text{InTe})$ composites.

SCEMT. Furthermore, its deviation of κ_L^* at 319 K is higher than that at 605 K, for example, 41% reduction at 319 K versus 33% reduction at 605 K, and are all going to be smaller as the x value increases. Finally the deviation gets zero at the end member of $\text{CuIn}_{0.7}\text{Ga}_{0.3}\text{Te}_2$ ($x = 0.3$). This estimation clearly indicates the presence of significant phonon scattering on the heterojunction at low temperatures.

To evaluate the possible phonon-scattering mechanism contributing to the large deviation from the estimation through EMT for the composite, we performed detailed microstructure investigations using high resolution transmission electron microscopy (HRTEM) on the sample CuInTe_2 :23 wt% InTe ($x = 0$). The results are shown in **Figure 6**, where Figure 6a–c is the EDS elemental mapping of Cu, In, and Te, and Figure 6d is the high-angle annular dark-field (STEM HAADF) image, which shows a high density of white nano strips $\text{CuIn}_x\text{Ga}_{1-x}\text{Te}_2$. The gray area is the blend of $\text{CuIn}_x\text{Ga}_{1-x}\text{Te}_2$ with InTe, which is hard to distinguish. Figure 6e is the high resolution TEM image, where many nano strips and domains are distributed in black or gray area, corresponding to the phase $\text{CuIn}_{1-x}\text{Ga}_x\text{Te}_2$. The size of the nano strips is 25–30 nm in width and 50–200 nm in length, and the domains ≈ 30 nm. Most nanoscale InTe phase is in situ formed along the phase boundaries (white area), which wraps the nano domains $\text{CuIn}_x\text{Ga}_{1-x}\text{Te}_2$, guided by yellow arrows in Figure 6e. Figure 6f is the magnified image of Figure 6e, where two phases $\text{CuIn}_{1-x}\text{Ga}_x\text{Te}_2$ and InTe are presented. The inset at the bottom left in Figure 6f is the FFT image, corresponding to the $\text{CuIn}_{1-x}\text{Ga}_x\text{Te}_2$ phase, while the one at the bottom right is the fast Fourier transform (FFT) confirming the InTe phase. Although the InTe phase at the interfaces does not play a dominant role in influencing the Seebeck coefficient, it acts as a phonon scattering unit (PSU), blocking the phonons of low and middle temperatures. The action is closely related to its own structure, as InTe exhibits an intrinsic bonding asymmetry with coexistent covalent and ionic substructures.^[48] That is why we have observed the reduced lattice part κ_L with InTe content increasing below 725 K. The schematic diagram is presented

in Figure 6g for better understanding the transports of phonons and electrons.

Because the anion position displacement (u) represents the degree of the lattice structure alteration on an atomic scale, its change has a profound impact on the phonon transport at high temperatures.^[50,51] However, the deviation of the u value in the main phase $\text{CuIn}_{1-x}\text{Ga}_x\text{Te}_2$ from 0.25 for each sample is almost the same (see Figure 1c), therefore, the extra phonon scattering caused by the crystal structure distortion should be limited. Besides, above ≈ 750 K, a relatively steep lowering of lattice thermal conductivity for the sample at $x = 0.3$ was observed, which is likely related to the order-disorder transition driven by the Cu-In antisite occupancy in the critical temperature range,^[52–54] as we did not identify any impurities at high temperatures from the high temperature XRD, see Figure S2, Supporting Information. However, the lattice part (κ_L) for the samples at $x \leq 0.2$ reduces almost linearly with temperature increasing. Therefore, it is concluded that the rapid reduction in κ_L and then convergence at high temperatures for the samples at $x \leq 0.2$ is mainly attributed to the phonon–phonon interaction and point defect scatterings introduced in the main phase $\text{CuIn}_{1-x}\text{Ga}_x\text{Te}_2$.

3. Conclusions

We have in this work prepared Ga-substituted Cu-In-Te ternary chalcogenides $\text{CuIn}_{1-x}\text{Ga}_x\text{Te}_2$: γInTe ($x = 0$ –0.3) and identified an in situ formed nanoscale phase InTe in the grain boundaries that decreases from 23.0 wt% ($x = 0$) to 0 ($x = 0.3$) in the matrix $\text{CuIn}_{1-x}\text{Ga}_x\text{Te}_2$. This nano phase InTe plays a predominant role in reducing the lattice thermal conductivity at low and middle temperatures. At high temperatures the phonon–phonon interaction and phonon scattering in point defects dominate at $x \leq 0.2$, thus leading to a reduction in κ_L by approximately a factor of 2 compared to CuInTe_2 reported. At the same time, the power factor increases by $\approx 73\%$, due to the narrowing of the bandgap (E_g) and the increasing of the DOS and effective mass. Consequently, the peak ZT value enhances to 1.22 at ≈ 850 K.

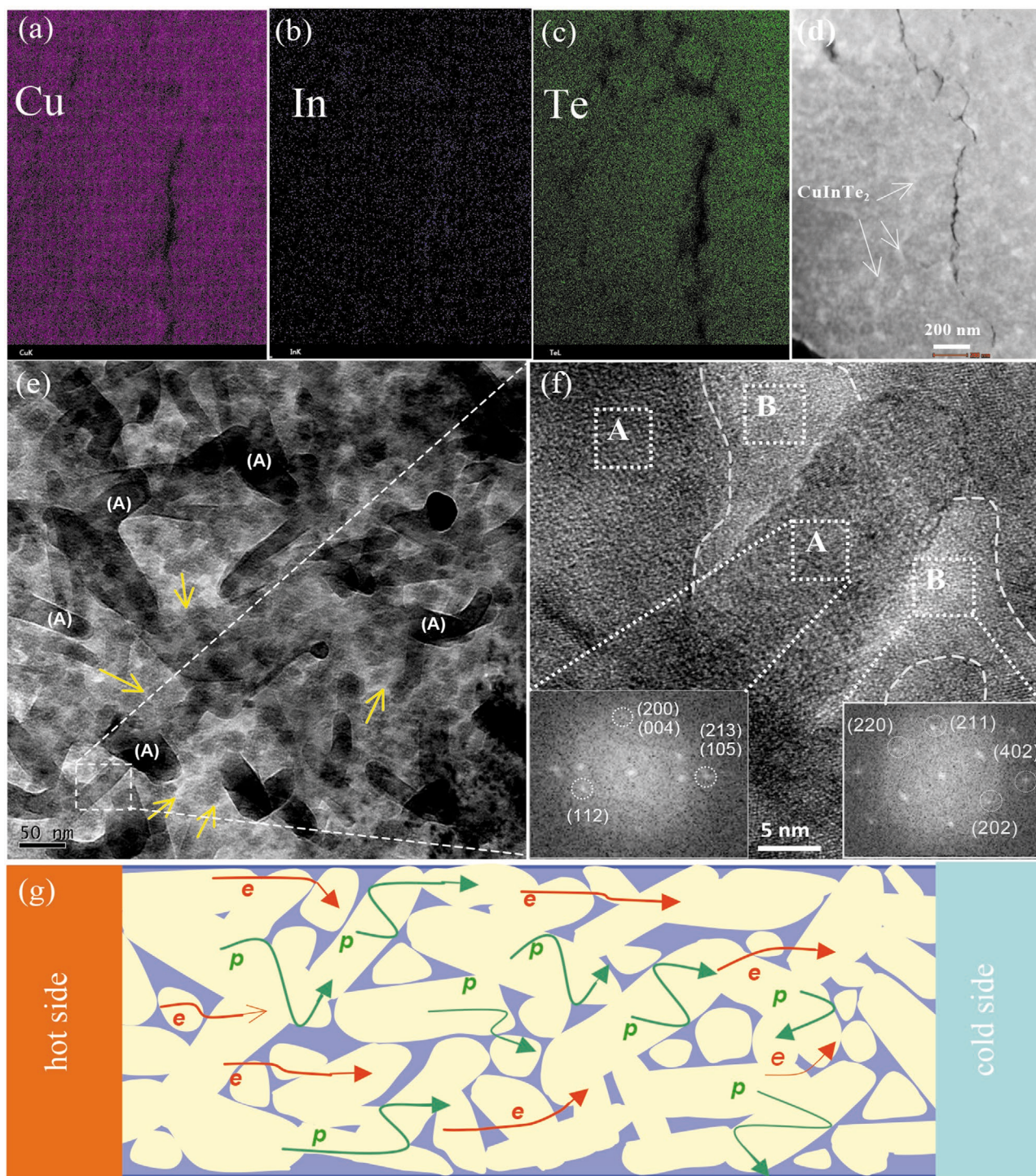


Figure 6. Microstructures of the bulk sample at $x = 0$. a–c) EDS mappings of elements, Cu, In, and Te; d) STEM HAADF (high-angle annular dark-field) image, which shows a relatively high density of white nano strips and domains corresponding to $\text{CuIn}_x\text{Ga}_{1-x}\text{Te}_2$; e) High resolution TEM image, where the nano strips and domains in black and/or gray area are distributed corresponding to $\text{CuIn}_{1-x}\text{Ga}_x\text{Te}_2$, signified by symbol A. The nanoscale InTe (symbol B) is in situ formed along the grain boundaries (white area), which wraps the nano domains $\text{CuIn}_x\text{Ga}_{1-x}\text{Te}_2$, guided by yellow arrows. f) Magnified TEM image, where two phases $\text{CuIn}_{1-x}\text{Ga}_x\text{Te}_2$ and InTe are presented. The lower left inset is the fast Fourier transform (FFT) of A, confirming the $\text{CuIn}_{1-x}\text{Ga}_x\text{Te}_2$ phase, while the lower right inset is the FFT image of B, which corresponds to the InTe phase. g) Schematic diagram illustrating the transport of both the phonons p and electrons e .

This value stands high in the CuInTe₂ or its based chalcogenides to date.

4. Experimental Section

Sample Preparation: The mixtures of four elements Cu, In, Ga, and Te (with the purity >99.999%, Emei Semicon. Mater. Co., Ltd. Sichuan, CN), according to the formula CuIn_{1-x}Ga_xTe₂:yInTe ($x = 0, 0.1, 0.2, 0.3$), were loaded into the different vacuum silica tubes. They were heated to 900 °C within 5 h, held at this temperature for 24 h, and then cooled down to room temperature (RT) in furnace. The dried powders were subsequently rapidly sintered using spark plasma sintering apparatus (SPS-1030) at a peak temperature of 900 K and a pressure of 50 MPa. The densities of the sintered bulks, ranging from 5.56 to $6.12 \times 10^{-3} \text{ kg cm}^{-3}$, were measured by using Archimedes' method.

The bulk samples about the size of $2.5 \times 3 \times 12 \text{ mm}^3$ were prepared for electrical property measurements, and those of $\phi 10 \times 1.5 \text{ mm}^2$ for thermal diffusivity measurement.

Physical Property Measurements: The Hall coefficient (R_H) at RT was measured using a PPMS (Model-9) with a magnetic field sweeping between $\pm 2.0 \text{ T}$. The Hall mobility (μ) and Hall carrier concentration (n_H) were subsequently determined based on the equations $\mu = |R_H|\sigma$ and $n_H = 1/(eR_H)$, respectively (e is the electron charge).

The Seebeck coefficients and electrical conductivities were evaluated by using ZEM-3 under a helium atmosphere at a temperature ranging from $\approx \text{RT}$ to 855 K with an uncertainty of <5.0% for each. The thermal diffusivities were measured using TC-1200RH with an uncertainty of <10.0%. The heat capacities (C_p) of the materials were just estimated in accordance with the Dulong–Petit rule, and are usually slightly lower than the real heat capacities, especially for the materials with nanograins that have large surface area.^[55] When calculating the electronic parts (κ_e) according to the equation $\kappa_e = L\sigma T$, the Lorenz numbers L were estimated using the formula $L = 1.5 + \exp(-|\alpha|/116)$,^[56] (where L is in $10^{-8} \text{ W } \Omega \text{ K}^{-2}$ and α in $\mu\text{V K}^{-1}$). The total uncertainty for ZT was $\approx 20\%$.

Structural Analyses: The powder X-ray diffraction patterns of the samples were registered using X-ray powder diffractometer (XRD) (D8 Advance) operating at 50 kV and 40 mA in a step size of 0.01° in the range of 10° to 100° , and a X'Pert Pro, PANalytical code was used to do the Rietveld refinement of the XRD patterns. The lattice constants were directly obtained from the refinement of the X-ray patterns using Jade software.

The microstructure of the bulk sample ($x = 0$) was examined by using high resolution transmission electron microscopy (HRTEM). HRTEM images were obtained at 220 kV using JEM-2010F (field emission TEM). The bulk sample used in TEM observations was prepared as follows. A small disc-shaped piece with an approximate size of $3 \times 3 \times 2 \text{ mm}$ was first cut from the spark plasma sintered disc using a low speed diamond wheel saw. The samples were finally thinned with a Gatan precision dimple grinder and then ion milled to electron transparency with a Gatan precision ion polishing system (PIPS).

Methodology: First-principles calculations of the compounds Cu₂₇In₃₃Te₆₄ and Cu₃₀In₃₀GaTe₆₄ were carried out with FHI-aims,^[57,58] an all-electron, full-potential electronic-structure code under the framework of density functional theory (DFT).^[59] FHI-aims use numeric atom-centered basis sets, where numerical settings are so chosen for the present study that a convergence in energy differences better than 10^{-3} eV per atom is achieved. Generalized gradient approximation (GGA) is used for electronic exchange and correlation as Perdew–Burke–Erzerhof (PBE).^[60] The electronic structure was calculated with more advanced Heyd–Scuseria–Ernzerhof hybrid functional (HSE06),^[61] which takes into account the fraction of exact exchange.

Supporting Information

Supporting Information is available from the Wiley Online Library or from the author.

Acknowledgements

This work was supported by the National Natural Science Foundation of China (51671109, 51171084).

Conflict of Interest

The authors declare no conflict of interest.

Keywords

chalcogenide CuIn_{1-x}Ga_xTe₂:yInTe, nanoscale phase InTe, phonons, electronic properties, synergistic regulation, thermoelectrics

Received: October 16, 2019

Revised: November 18, 2019

Published online:

- [1] R. Liu, L. Xi, H. Liu, X. Shi, W. Zhang, L. Chen, *Chem. Commun.* **2012**, 48, 3818.
- [2] A. Kosuga, T. Plirdpring, R. Higashine, M. Matsuzawa, K. Kurosaki, S. Yamanaka, *Appl. Phys. Lett.* **2012**, 100, 042108.
- [3] J. Wei, H. Liu, L. Cheng, J. Zhang, J. H. Liang, P. H. Jiang, D. D. Fan, J. Shi, *AIP Adv.* **2015**, 5, 107230.
- [4] M. V. Yakushev, A. V. Mudryi, E. Kärber, P. R. Edwards, R. W. Martin, *Appl. Phys. Lett.* **2019**, 114, 062103.
- [5] T. J. Scheidemantel, C. Ambrosch-Draxl, T. Thonhauser, J. V. Badding, J. O. Sofo, *Phys. Rev. B* **2003**, 68, 125210.
- [6] N. F. Hinsche, B. Yu, Yavorsky, M. Gradhand, M. Czerner, M. Winkler, J. König, H. Bottner, I. Mertig, P. Zahn, *Phys. Rev. B* **2012**, 86, 085323.
- [7] J. O. Dimmock, I. Melngailis, A. J. Strauss, *Phys. Rev. Lett.* **1966**, 16, 1193.
- [8] Y. Pei, H. Wang, G. J. Snyder, *Adv. Mater.* **2012**, 24, 6125.
- [9] Z. Xia, G. Wang, X. Zhou, W. Wen, *Ceram. Int.* **2017**, 43, 16276.
- [10] R. Liu, Y. Qin, N. Cheng, J. Zhang, X. Shi, Y. Grin, L. Chen, *Inorg. Chem. Front.* **2016**, 3, 1167.
- [11] N. Cheng, R. Liu, S. Bai, X. Shi, L. Chen, *J. Appl. Phys.* **2014**, 115, 163705.
- [12] G. A. Slack, in *CRC Handbook of Thermoelectrics* (Ed: M. Rowe), CRC, Boca Raton, FL **1995**, pp. 407–440.
- [13] Y. Tang, Z. M. Gibbs, L. A. Agapito, G. Li, H. S. Kim, M. B. Nardelli, S. Curtarolo, G. J. Snyder, *Nat. Mater.* **2015**, 14, 1223.
- [14] Y. Pei, X. Shi, A. LaLonde, H. Wang, L. Chen, G. J. Snyder, *Nature* **2011**, 473, 66.
- [15] J. P. Heremans, V. Jovic, E. S. Toberer, A. Saramat, K. Kurosaki, A. Charoenphakdee, S. Yamanaka, G. J. Snyder, *Science* **2008**, 321, 554.
- [16] W. Zhao, Z. Liu, Z. Sun, Q. Zhang, P. Wei, X. Mu, H. Zhou, C. Li, S. Ma, D. He, P. Ji, W. Zhu, X. Nie, X. Su, X. Tang, B. Shen, X. Dong, J. Yang, Y. Liu, J. Shi, *Nature* **2017**, 549, 247.
- [17] J. Vaney, S. A. Yamini, H. Takaki, K. Kobayashi, N. Kobayashi, T. Mori, *Mater. Today Phys.* **2019**, 9, 100090.
- [18] N. Tsujii, A. Nishide, J. Hayakawa, T. Mori, *Sci. Adv.* **2019**, 5, eaat5935.
- [19] F. Ahmed, N. Tsujii, T. Mori, *J. Mater. Chem. A* **2017**, 5, 7545.
- [20] K. Biswas, J. He, I. D. Blum, C.-I. Wu, T. P. Hogan, D. N. Seidman, V. P. Dravid, M. G. Kanatzidis, *Nature* **2012**, 489, 414.
- [21] Y. Luo, J. Yang, Q. Jiang, W. Li, Y. Xiao, L. Fu, D. Zhang, Z. Zhou, Y. Cheng, *Nano Energy* **2015**, 18, 37.
- [22] Y. Luo, Q. Jiang, J. Yang, W. Li, D. Zhang, Z. Zhou, Y. Cheng, Y. Ren, X. He, X. Li, *Nano Energy* **2017**, 32, 80.

- [23] T. Mori, *Small* **2017**, *13*, 1702013.
- [24] W. Li, L. Zheng, B. Ge, S. Lin, X. Zhang, Z. Chen, Y. Chang, Y. Pei, *Adv. Mater.* **2017**, *29*, 1605887.
- [25] Y. Xiao, H. Wu, W. Li, M. Yin, Y. Pei, Y. Zhang, L. Fu, Y. Chen, S. J. Pennycook, L. Huang, J. He, L. Zhao, *J. Am. Chem. Soc.* **2017**, *139*, 18732.
- [26] Z. Liu, J. Mao, T. Liu, G. Chen, Z. Ren, *MRS Bull.* **2018**, *43*, 181.
- [27] J. Mao, Z. Liu, J. Zhou, H. Zhu, Q. Zhang, G. Chen, Z. Ren, *Adv. Phys.* **2018**, *67*, 69.
- [28] J. He, T. M. Tritt, *Science* **2017**, *357*, 1369.
- [29] J. Zhang, R. Liu, N. Cheng, Y. Zhang, J. Yang, C. Uher, X. Shi, L. Chen, W. Zhang, *Adv. Mater.* **2014**, *26*, 3848.
- [30] J. Yang, S. Chen, Z. Du, X. Liu, J. Cui, *Dalton Trans.* **2014**, *43*, 15228.
- [31] Y. Luo, J. Yang, Q. Jiang, W. Li, D. Zhang, Z. Zhou, Y. Cheng, Y. Ren, X. He, *Adv. Energy Mater.* **2016**, *6*, 1600007.
- [32] W. Li, Y. Luo, Y. Zheng, C. Du, Q. Liang, B. Zhu, L. Zhao, *J. Mater. Sci.* **2018**, *29*, 4732.
- [33] M. Li, Y. Luo, G. Cai, X. Li, X. Li, Z. Han, X. Lin, D. Sarker, J. Cui, *J. Mater. Chem. A* **2019**, *7*, 2360.
- [34] T. Ren, P. Ying, G. Cai, X. Li, Z. Han, L. Min, J. Cui, *RSC Adv.* **2018**, *8*, 27163.
- [35] T. Ren, Z. Han, P. Ying, X. Li, X. Li, X. Lin, D. Sarker, J. Cui, *ACS Appl. Mater. Interfaces* **2019**, *11*, 32192.
- [36] Y. M. Zhou, H. J. Wu, Y. L. Pei, C. Chang, Y. Xiao, X. Zhang, S. K. Gong, J. Q. He, L. D. Zhao, *Acta Mater.* **2017**, *125*, 542.
- [37] J. E. Jaffe, A. Zunger, *Phys. Rev. B* **1984**, *29*, 1882.
- [38] S. B. Zhang, S. H. Wei, A. Zunger, *Phys. Rev. B* **1998**, *57*, 9642.
- [39] H. Chen, C. Yang, H. Liu, G. Zhang, D. Wan, F. Huang, *CrystEng-Comm* **2013**, *15*, 6648.
- [40] Z. Xia, G. Wang, X. Zhou, W. Wen, *Mater. Res. Bull.* **2018**, *101*, 184.
- [41] G. Zhou, D. Wang, *Phys. Chem. Chem. Phys.* **2016**, *18*, 5925.
- [42] W. D. Carr, D. T. Morelli, *J. Alloys Compd.* **2015**, *630*, 277.
- [43] B. Wang, H. Xiang, T. Nakayama, J. Zhou, B. Li, *Phys. Rev. B* **2017**, *95*, 035201.
- [44] G. J. Snyder, E. S. Toberer, *Nat. Mater.* **2008**, *7*, 105.
- [45] Y. Lan, A. J. Minnich, G. Chen, Z. Ren, *Adv. Funct. Mater.* **2010**, *20*, 357.
- [46] Y. Pei, A. D. LaLonde, N. A. Heinz, X. Shi, S. Iwanaga, H. Wang, L. Chen, G. J. Snyder, *Adv. Mater.* **2011**, *23*, 5674.
- [47] V. Kucek, C. Drasar, J. Kasparova, T. Plechacek, J. Navratil, M. Vlcek, L. Benes, *J. Appl. Phys.* **2015**, *118*, 125105.
- [48] M. K. Jana, K. Pal, U. V. Waghmare, K. Biswas, *Angew. Chem., Int. Ed.* **2016**, *55*, 7792.
- [49] Z. Hashin, S. Shtrikman, *J. Appl. Phys.* **1962**, *33*, 3125.
- [50] J. Cui, Y. Li, Z. Du, Q. Meng, H. Zhou, *J. Mater. Chem. A* **2013**, *1*, 677.
- [51] W. Wu, Y. Li, Z. Du, Q. Meng, Z. Sun, W. Ren, J. Cui, *Appl. Phys. Lett.* **2013**, *103*, 011905.
- [52] A. Zunger, *Appl. Phys. Lett.* **1987**, *50*, 164.
- [53] S. Schorr, G. Geandier, B. V. Korzun, *Phys. Status Solidi C* **2006**, *3*, 2610.
- [54] C. Rincón, *Solid State Commun.* **1987**, *64*, 663.
- [55] M. Kim, W. Lee, K. Cho, J. Ahn, Y. Sung, *ACS Nano* **2016**, *10*, 7197.
- [56] H. Kim, Z. M. Gibbs, Y. Tang, H. Wang, G. J. Snyder, *APL Mater.* **2015**, *3*, 041506.
- [57] V. Blum, R. Gehrke, F. Hanke, P. Havu, V. Havu, X. Ren, K. Reuter, M. Scheffler, *Comput. Phys. Commun.* **2009**, *180*, 2175.
- [58] P. Hohenberg, W. Kohn, *Phys. Rev.* **1964**, *136*, B864.
- [59] W. Kohn, L. J. Sham, *Phys. Rev.* **1965**, *140*, A1133.
- [60] J. P. Perdew, K. Burke, M. Ernzerhof, *Phys. Rev. Lett.* **1996**, *77*, 3865.
- [61] A. V. Krukau, O. A. Vydrov, A. F. Izmaylov, G. E. Scuseria, *J. Chem. Phys.* **2006**, *125*, 224106.